Inorganic Chemistry

pubs.acs.org/IC Article

Synthetic Metallodithiolato Ligands as Pendant Bases in [Fe^{I}Fe^{I}], [Fe^{I}[Fe(NO)]^{II}], and [(μ-H)Fe^{II}Fe^{II}] Complexes

Kavindu Dilshan Kariyawasam Pathirana, Pokhraj Ghosh, Chung-H. Hsieh, Lindy Chase Elrod, Nattamai Bhuvanesh, Donald J. Darensbourg,* and Marcetta Y. Darensbourg*

Cite This: *Inorg. Chem.* 2020, 59, 3753−3763 Read Online

ACCESS | Metrics & More | Article Recommendations | Supporting Information

ABSTRACT: The development of ligands with specific stereo- and electrochemical requirements that are necessary for catalyst design challenges synthetic chemists in academia and industry. The crucial azadithiolate linker in the active site of [FeFe]-H_2ase has inspired the development of synthetic analogues that utilize ligands which serve as conventional σ donors with pendant base features for H^+ binding and delivery. Several MN_2S_2 complexes (M = Ni^{2+}, $[Fe(NO)]^{2+}$, $[Co(NO)]^{2+}$, etc.) utilize these cis-dithiolates to bind low valent metals and also demonstrate the useful property of hemilability, i.e., alternate between bi- and monodentate ligation. Herein, synthetic efforts have led to the isolation and characterization of three heterotrimetallics that employ metallodithiolato ligand binding to di-iron scaffolds in three redox levels, (μ-pdt)$[Fe(CO)_3]_2$, (μ-pdt)$[Fe(CO)_3][(Fe(NO))^{II}(IMe)(CO)]^+$, and ($\mu$-pdt)($\mu$-H)$[Fe^{II}(CO)_2(PMe_3)]_2^+$ to generate (μ-pdt)$[(Fe^{I}(CO)_3][Fe^{I}(CO)_2{\cdot}NiN_2S_2]$ (**1**), (μ-pdt)$[Fe^{I}(CO)_3][(Fe(NO))^{II}(IMe)(CO)]^+$ (**2**), and (μ-pdt)(μ-H)$[Fe^{II}(CO)_2(PMe_3)][Fe^{II}(CO)(PMe_3){\cdot}NiN_2S_2]^+$ (**3**) complexes (pdt = 1,3-propanedithiolate, IMe = 1,3-dimethylimidazole-2-ylidene, NiN_2S_2 = [N,N′-bis(2-mercaptoethyl)-1,4-diazacycloheptane] nickel(II)). These complexes display efficient metallodithiolato binding to the di-iron scaffold with one thiolate-S, which allows the free unbound thiolate to potentially serve as a built-in pendant base to direct proton binding, promoting a possible Fe−$H^-\cdots{}^+$H−S coupling mechanism for the electrocatalytic hydrogen evolution reaction (HER) in the presence of acids. Ligand substitution studies on **1** indicate an associative/dissociative type reaction mechanism for the replacement of the NiN_2S_2 ligand, providing insight into the Fe−S bond strength.

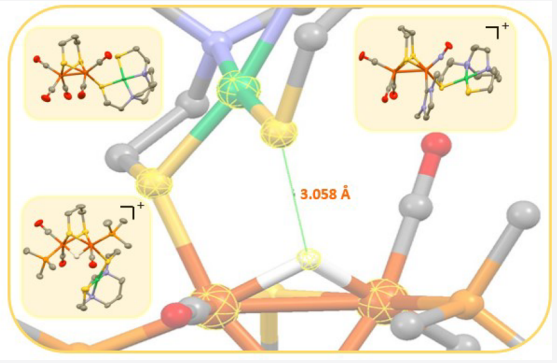

INTRODUCTION

The search for innovative ligands to meet specific stereo- and electrochemical requirements in catalyst development is of imminent interest to synthetic chemists. Biomimetics of the hydrogenase active sites have provided particular challenges and opportunities to explore fundamental properties of abiotic ligands that might provide function to the small molecules similar to that of the metalloenzymes that exist with many layers of control via the protein matrix.[1−5] The two most prominent hydrogenases, [FeFe]- and [NiFe]-H_2ase, are thiolate-S bridged bimetallics, with diatomics attached to iron, CN^-, and CO, in both.[1,6,7] Hence, for biomimetic purposes, organometallic chemists have used familiar ligands such as phosphines and N-heterocyclic carbenes, of similar donor ability to CN^-, but having the advantage that they avoid the problem of ligand-based, i.e., cyanide-nitrogen, protonation that does not direct the proton toward iron, an ultimate requirement for H^+/H^- coupling.[5−8] Such proton shuttling capability is readily arranged by the proteins, via an azadithiolate in the [FeFe]-H_2ase; a terminal cysteinyl sulfur operates in this function for the [NiFe]-H_2ase.[9]

We have long had interest in metallodithiolato ligands, particularly MN_2S_2.[10] As *cis*-dithiolates, they are generally found as bidentate ligands creating M(μ-S)$_2$M″ butterfly type structures.[10,11] These ligands are tunable based on the hydrocarbon linkers between S and N and between N and N, as well as the characteristics of the central metal, M.[10] The most common of these are square planar MN_2S_2 with M = Ni^{II}; however square pyramidal systems (M = $(V{\equiv}O)^{2+}$, $[(NO)Fe]^{II}$ or $[(NO)Co]^{II}$) are also known to act as sulfur donor based metallo-ligands to various receivers, particularly low valent metals with additional carbonyl or nitrosyl ligands.[12]

Several bimetallic complexes have been developed in various laboratories as electrocatalysts for the hydrogen evolution reaction, HER, despite the absence of a well-positioned pendant base as a proton shuttle.[13−16] Nevertheless, computa-

Received: November 20, 2019
Published: February 21, 2020

Downloaded via TEXAS A&M UNIV COLG STATION on October 26, 2020 at 20:32:20 (UTC).
See https://pubs.acs.org/sharingguidelines for options on how to legitimately share published articles.

© 2020 American Chemical Society

https://dx.doi.org/10.1021/acs.inorgchem.9b03409
Inorg. Chem. 2020, 59, 3753−3763

tional studies aimed at exploring the mechanism of proton/electron coupling according to the electrochemical events displayed on the acid concentration-dependent cyclic voltammograms indicated that one of the guiding principles was the actuation of hemilability, Figure 1.[17] As shown in

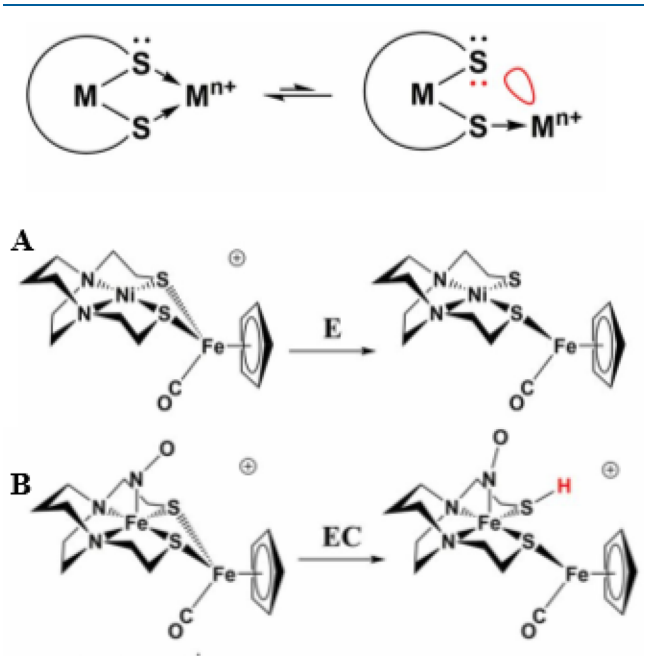

Figure 1. Hemilability in MN_2S_2 bridging thiolates.[17]

Figure 1, dissociation of one dative RS → M bond opens up two reactive sites: a base on thiolate sulfur and a hole on the M available for the addition of an electron. Specific examples are presented in Figure 1; pathway A indicates the addition of an electron, first to the open space on the 16-electron Ni^{II} side of the bimetallic. A fast electron transfer to the more electrophilic iron reduces Fe^{II} to Fe^{I} and opens the Fe−S bond. The B route indicates that the first added electron, buffered by the electron-delocalizing NO ligand, is insufficient to induce hemilability, but rather both an electron and proton are needed prior to S−Fe bond cleavage.[12] In this way, the MN_2S_2 ligands may create a temporary but necessary pendant base, avoiding the synthetic requirement of building a permanently available strategically located Lewis base.[17]

Synthetic analogues of the [2Fe2S] active site of [FeFe]-H_2ase provide a unique opportunity to explore the influences of specific changes in binuclear complexes. Previous studies on the ubiquitous $(\mu\text{-pdt})[Fe(CO)_3]_2$ concluded that rates of CO/CN^- ligand substitution processes correlate with fluxionality in the $Fe(CO)_3$ rotors, that is, the intramolecular CO_{ap}/CO_{ba} site exchange on individual metals.[18−20] Such rotation, likely promoted by an incoming ligand, coupled with shifting the electron density in the Fe−Fe bond, leads to an open site readily available to said donor, with concomitant release of a CO (SI Figure S12).[18] In this way, an associative mechanism for ligand substitution on a pseudo 18-electron metal center is made possible, on individual and alternate iron centers. The monosubstituted $(\mu\text{-pdt})[Fe(CO)_3][Fe(CO)_2CN]^-$ is followed by the second process and yields the much appreciated disubstituted dianion $(\mu\text{-pdt})[Fe(CO)_2CN]_2^{2-}$.[20] Phosphine mimics of this process lead to the analogous $(\mu\text{-pdt})[Fe^{I}(CO)_2PR_3]_2$, which is capable of taking up a proton in a binuclear oxidative addition reaction, yielding the bridging hydride, $(\mu\text{-pdt})(\mu\text{-H})[Fe^{II}(CO)_2PR_3]_2^+$, with oxidation state conversions of Fe^{I} to Fe^{II}.[21] While these CO/L substitution reactions are on alternate iron centers, in another study it was found that the nitrosonium ligand, NO^+, isoelectronic with CO but greater engendering electron deficiency on the metal to which it adds, promotes a second CO/L exchange on the same iron.[22] That is, a completely dissymmetric di-iron complex is produced: $(\mu\text{-pdt})[Fe(CO)_3][Fe(L')(NO)(L)]^+$ where L = N-heterocyclic carbene or phosphine. Notably, the NO^+ ligand effectively oxidizes one iron in the di-iron complex, giving the opportunity to contrast di-iron complexes in three redox levels, $Fe^{I}Fe^{I}$, $Fe^{I}Fe^{II}$, and $Fe^{II}Fe^{II}$. We have attempted using the NiN_2S_2 metalloligand as a surrogate for phosphine or NHC in di-iron complexes. We are particularly interested in assessing whether the metalloligand binds in bidentate or monodentate fashion, and if the latter, how does the unbound thiolate orient itself when twisted away from the first coordination sphere. Thus, the trimetallic complexes were synthesized and characterized by XRD: $(\mu\text{-pdt})[Fe^{I}(CO)_3][Fe^{I}(CO)_2\cdot NiN_2S_2]$ (**1**), $(\mu\text{-pdt})[Fe^{I}(CO)_3][\{Fe(NO)\}^{II}(IMe)\cdot NiN_2S_2]^+BF_4^-$ (**2**), and $(\mu\text{-pdt})(\mu\text{-H})[Fe^{II}(CO)_2(PMe_3)]-[Fe^{II}(CO)(PMe_3)\cdot NiN_2S_2]^+PF_6^-$ (**3**). Complex **1** was examined for the response of the cyclovoltammogram to added equivalents of acid, i.e., for indications of electrocatalytic proton reduction. Furthermore, a kinetic analysis of NiN_2S_2 ligand displacement in an attempt to obtain a measure of the Fe−S bond strength of the neutral complex **1** was also performed. Throughout this manuscript, NiN_2S_2 refers to the [N,N′-bis(2-mercaptidoethyl)-1,4-diazacycloheptane] nickel-(II) complex.

RESULTS AND DISCUSSION

Synthesis. *Complex 1.* Scheme 1 describes the synthetic protocol employed to obtain the three complexes of this study. Direct combination of the $(\mu\text{-pdt})[Fe^{I}(CO)_3]_2$ parent compound with NiN_2S_2 over the course of 1 h showed negligible reaction even on heating. However, with addition of the decarbonylating agent Me_3NO, the solution color immediately changed from red to dark brown with a release of CO_2, giving the desired complex **1** (Scheme 1). Infrared spectroscopy showed a bathochromic shift of ν(CO) stretching frequencies to 2032(s), 1962(s), and 1900(w) upon binding of the σ-donating NiN_2S_2 ligand (ν(CO) of $(\mu\text{-pdt})[Fe^{I}(CO)_3]_2$: 2072(m), 2037(s), 1990(s)). The pattern of ν(CO) stretching frequencies matched that of the $(\mu\text{-pdt})[Fe^{I}(CO)_3]-[Fe^{I}(CO)_2PR_3]$ species, indicative of monodentate binding of the NiN_2S_2 ligand to the di-iron core (Table 1). The slight lowering of ν(CO) values of complex **1** vs $(\mu\text{-pdt})[Fe^{I}(CO)_3]-[Fe^{I}(CO)_2PR_3]$ indicates that the NiN_2S_2 metallodithiolato ligand is a better donor than phosphines.[23,24] Nevertheless, the addition of PMe_3 to **1** results in displacement of the NiN_2S_2 ligand, forming $(\mu\text{-pdt})[Fe^{I}(CO)_3][Fe^{I}(CO)_2PMe_3]$, **1**-$PMe_3$. It is interesting to note that, unlike NiN_2S_2, PMe_3 reacts directly with the parent compound $(\mu\text{-pdt})[Fe^{I}(CO)_3]_2$ without the need for oxidative assistance in the elimination of CO. As the NiN_2S_2 is a better electron-donating ligand than PMe_3, we postulate that this discrepancy is due to the larger steric hindrance from NiN_2S_2 in the associative substitution process.

Complex 2. On mixing the parent compound $(\mu\text{-pdt})[Fe-(CO)_3][(Fe(NO))^{II}(IMe)(CO)]^+BF_4^-$ with NiN_2S_2, a clean conversion led to the paramagnetic complex **2** (Scheme 1) that

https://dx.doi.org/10.1021/acs.inorgchem.9b03409
Inorg. Chem. 2020, 59, 3753−3763

Scheme 1. Synthesis of Complexes 1, 2, and 3

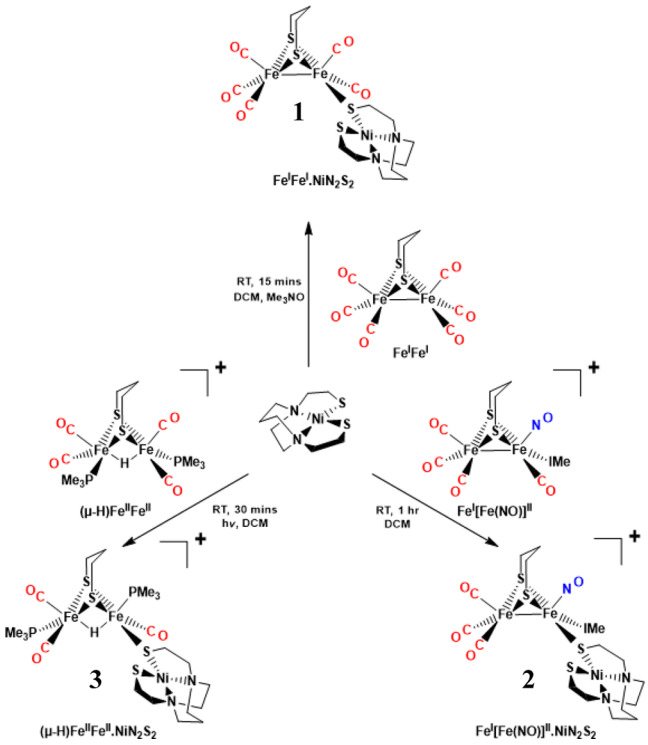

Table 1. IR Stretching Frequencies for Complexes 1, 2, and 3 and Starting Materials and Their Corresponding Monosubstituted Phosphine Derivatives

complexes	diatomic vibrational frequencies (cm^{-1})[a]
[Fe^IFe^I]	
$(\mu\text{-pdt})[Fe^I(CO)_3]_2$	2072(m), 2037(s), 1990(s)[b,25]
$(\mu\text{-pdt})[Fe^I(CO)_3][Fe^I(CO)_2(PPh_3)]$	2044(s), 1984(s), 1931(m)[b,26]
$(\mu\text{-pdt})[Fe^I(CO)_3][Fe^I(CO)_2(NiN_2S_2)]$ (**1**)	2032(s), 1962(s), 1900(w)[c,d]
[$Fe^I(Fe(NO))^{II}$]	
$(\mu\text{-pdt})[Fe^I(CO)_3][(Fe(NO))^{II}(IMe)(CO)]^+$	2085(s), 2058(s), 2018(s), 1809(s)[c,22]
$(\mu\text{-pdt})[Fe^I(CO)_3][(Fe(NO))^{II}(IMe)(PMe_3)]^+$	2061(s), 1996(s), 1759(m)[c,22]
$(\mu\text{-pdt})[Fe^I(CO)_3][(Fe(NO))^{II}(IMe)(NiN_2S_2)]^+$ (**2**)	2056(s), 1990(s), 1740(m)[c,d]
(μ-H)[$Fe^{II}Fe^{II}$]	
(μ-H) $(\mu\text{-pdt})[Fe^{II}(CO)_2(PMe_3)]_2^+$	2032(s), 1990(s)[c,21]
(μ-H) $(\mu\text{-pdt})[Fe^{II}(CO)_2(PMe_3)][Fe^{II}(CO)(PMe_3)(NiN_2S_2)]^+$ (**3**)	2023(s), 1968(m), 1929(m)[c,d]

[a]Values underlined are for NO. [b]Spectra measured in CH_3CN. [c]Spectra measured in CH_2Cl_2. [d]This work.

contains a fully substituted iron. Consistent with the better donor ability of NiN_2S_2, similar bathochromic shifts in ν(CO) and ν(NO) stretching frequencies were observed. The X-band EPR spectra of complex **2**, collected in perpendicular mode field polarization in CH_2Cl_2 solutions at 298 K, showed the presence of an $S = 1/2$ species with a $g_\perp$ value of 2.09 (Figure 2B). It is important to note that the NiN_2S_2 ligand substitutes the CO on the $[\{Fe(NO)\}^{II}(IMe)(CO)]$ center without any external assisance from a reagent such as Me_3NO, unlike in the case of complex **1**. Furthermore, in terms of steric hindrance, it

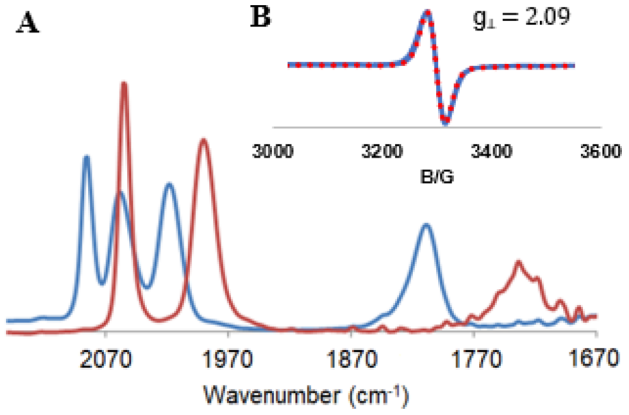

Figure 2. (A) Overlay of IR spectra recorded in CH_2Cl_2 solution of **2** (red) and the $(\mu\text{-pdt})[Fe^I(CO)_3][\{Fe(NO)\}^{II}(IMe)(CO)]^+BF_4^-$ (blue) starting material. (B) CH_2Cl_2 solution EPR spectra of **2** at 298 K The g value reported is from a simulation shown in the red trace.

seems unlikely that the NiN_2S_2 would react easily with the iron center that already contains a bulky IMe ligand. N-heterocyclic carbene (IMes or IMe) stabilized $(\mu\text{-pdt})[Fe^I(CO)_3][\{Fe(NO)\}^{II}(IMe)L]^+$ complexes have been previously studied with respect to CO exchange (within the $[(Fe(NO))^{II}(CO)L]$ moiety) using PMe_3 and CN^-, which seem to react similarly to NiN_2S_2. The redox noninnocent ligand NO of the parent compound creates a $\{FeNO\}^7$ unit in the $[\{Fe(NO)\}^{II}(IMe)(CO)]$ center. Together with the electron withdrawing capability of NO, the $[\{Fe(NO)\}^{II}(IMe)(CO)]$ center presents a better electrophile compared to the $[Fe(CO)_3]$ center to the incoming NiN_2S_2 ligand, which leads to the formation of trisubstituted iron.

Complex 3. Photolysis by sunlamp irradiation of $(\mu\text{-pdt})(\mu\text{-H})[Fe^{II}(CO)_2(PMe_3)]_2^+PF_6^-$ in the presence of NiN_2S_2 formed complex **3**, over a period of 30 min in CH_2Cl_2 (Scheme 1). The change in pattern and position of ν(CO) values, from 2032 and 1990 to 2023, 1968, and 1929 cm^{-1} reflects the increase in electron density in the di-iron core, upon binding of NiN_2S_2 (Table 1). Thus, CO substitution results in a tricarbonyl species making use of a metal-lodithiolato ligand, NiN_2S_2, as has been established using neutral or anionic σ-donor ligands. It is important to note that the visible light irradiation is required to drive the reaction forward. Complexes similar to $(\mu\text{-pdt})(\mu\text{-H})[Fe^{II}(CO)_2(PMe_3)]_2^+PF_6^-$ are known to eject a CO ligand upon photolysis, producing an open site for the incoming ligand. During the formation of complex **2**, NiN_2S_2 readily reacts with the $[\{Fe(NO)\}^{II}(IMe)(CO)]$ center without any chemical/physical assistance to remove one of its CO's to generate a fully substituted iron center. However, formally being in the Fe^{II} oxidation state, parent compound $(\mu\text{-pdt})(\mu\text{-H})[Fe^{II}(CO)_2(PMe_3)_2]^+PF_6^-$ requires photolysis in order to create an open site for the incoming NiN_2S_2.

X-ray Diffraction Analysis. X-ray quality crystals of complexes **1**, **2**, and **3** were obtained by layering concentrated CH_2Cl_2 solutions with hexane at −28 °C under nitrogen. All three complexes show monodentate binding of the NiN_2S_2 ligand to the di-iron unit. The distance between the bound sulfur and iron is around 2.3 Å, and the distance between nonbound sulfur and the nearest iron within the trimetallic is around 4 Å in all complexes (Figure 3). The Ni^{II} in the

https://dx.doi.org/10.1021/acs.inorgchem.9b03409
Inorg. Chem. 2020, 59, 3753−3763

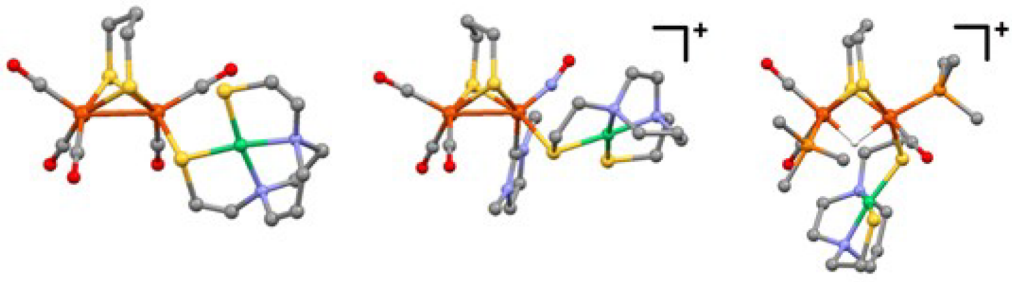

(1) (2) (3)

Figure 3. Crystal structures of **1**, **2** as its BF_4^- salt, and **3** as its BAr^{F-} salt.

metalloligand is maintained within a square planar geometry, and the Ni···$Fe_{proximal}$ distances are around 3.6 Å. (Table 2)

Table 2. Selected Metric Parameters of 1, 2, and 3

	1	2	3
Fe−Fe/Å	2.551 (2)	2.592 (9)	2.579 (8)
Fe−S_b*/Å[a]	2.308 (4)	2.369 (9)	2.326 (1)
Fe−S_{nb}*/Å[b]	3.843 (5)	3.916 (1)	3.995 (2)
S*−S*/Å[c]	3.197 (5)	3.206 (1)	3.206 (2)
Ni_{disp}/Å[d]	0.020	0.013	0.057
S*−Ni−S*/deg	93.6 (1)	95.03 (4)	94.9 (1)

[a]Fe-bonding sulfur distance. [b]Fe-nonbonding sulfur distance. [c]Sulfur−sulfur distance in NiN_2S_2. [d]Displacement of Ni from N_2S_2 best plane.

Complex **1** shows that NiN_2S_2 binds to the iron center from a basal position with an Fe···S_b distance of 2.30 Å. The $FeS_2(C_{CO})_2S_{NiN_2S_2}$ moiety of **1** is square pyramidal (τ = 0.03) The best plane of NiN_2S_2 is moderately coplanar with the FeS_pFe (where S_p is the S of pdt, proximal to NiN_2S_2) plane for complex **1**.

Complex **2** shows that the NiN_2S_2 binds to the iron center from the basal position of the pseudosquare pyramidal Fe. The Fe−Fe distance is slightly elongated (0.03 Å) compared to the analogous CN^- derivative. Due to the steric hindrance on the substituted iron side, both the flap of the pdt unit and the Fe−N−O angle are bent toward the unsubstituted iron. The torsion angles, defined by N_{ap}−Fe−Fe−C_{ap}, are ∼7° for complex **2** and the reported CN^- derivative, while it is much lower, ∼1°, for the reported PMe_3 derivative. Conversely, the τ value for the substituted Fe shows a discernible square pyramidal geometric distortion for complex **2** and the reported PMe_3 derivative (0.22 and 0.26, respectively), while the reported CN^- substituted complex maintains a moderately regular square pyramid (τ = 0.1). This can be attributed to the steric interference from the PMe_3 and the metallodithiolato ligand as compared to the linear diatomic cyanide. The Ni^{II}, present in a perfect square plane, is 3.4 Å away from the proximal Fe, negating any bonding interaction (Table 2).

In complex **3**, substitution of CO by NiN_2S_2 in (μ-pdt)(μ-H)$[Fe^{II}(CO)_2(PMe_3)]_2^+$ repositions the PMe_3 ligands from trans-basal to apical-basal, minimizing the steric interactions between the NiN_2S_2 and PMe_3. The flap created by the pdt is oriented toward the disubstituted iron. Unlike other complexes, NiN_2S_2 positions itself in a manner such that the N_2S_2 plane is oriented toward the di-iron scaffold in complex **3**, thereby shortening the free-thiolate to potential bridging-hydride distance to 3.06 Å (Table 2). This feature serves as a potential structural platform to the "free thiolate as a pendant base" thesis, such that the unbound thiolate can hold a proton for a convenient proton/hydride coupling in dihydrogen formation.

Electrochemistry. Complex **1** is the most well-behaved, and its stability permits further electrochemical analysis. Complex **2** is quite unstable, especially in the presence of acid, and the opposite is the case with complex **3** and its very stable bridging hydride. Two irreversible reductions (E_{pc}) at −1.82 V and −2.1 V are assigned for Fe^IFe^I/Fe^IFe^0 and Fe^IFe^0/Fe^0Fe^0 couples, respectively[27] (Figure 4). The starting material (μ-pdt)$[Fe(CO)_3]_2$ shows two irreversible reductions similarly at −1.34 V and −1.95 V,[25] and it is reasonable to assume that in complex **1** the shift in reduction potentials toward a more negative value is due to the electron-donating capability of the appended NiN_2S_2 ligand, which increases the electron density at the di-iron core similarly to the (μ-pdt)$[Fe(CO)_3][Fe(CO)_2PMe_3]$.[27] Similar trends have been observed in complexes such as (μ-pdt)$[Fe(CO)_2(PMe_3)]_2$, where a single reduction event corresponding to the Fe^IFe^I/Fe^IFe^0 couple occurs at −1.85 V.[25] A quasi-reversible reduction event is formed at −2.41 V, which corresponds to $Ni^{II/I}$ reduction (SI Figure S9). Bimetallic complexes that are composed of a metallodithiolato ligand and a Lewis acidic metal center usually show a positive shift in the reduction potential of the metal center in the metallodithiolato ligand due to the decrease in electron density around it.[10] However, the reduction potential of Ni in complex **1** shows no significant shift compared to free NiN_2S_2.[28] One possible reason for this might be the initial reduction of the di-iron core prior to the Ni reduction. The effect of the reduced iron on the reduction

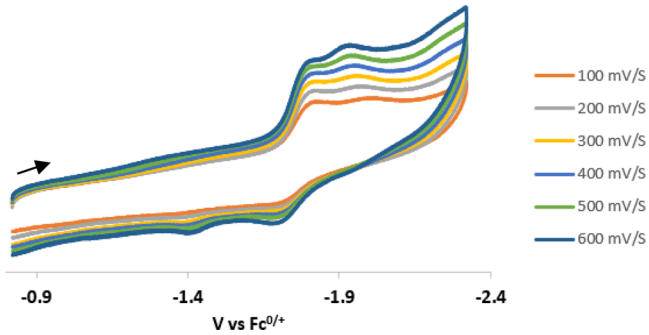

Figure 4. Scan rate dependence of complex **1** as a 2.0 mM CH_3CN solution containing 0.1 M $[^tBu_4N][PF_6]$. (Scans were initiated in negative direction.)

https://dx.doi.org/10.1021/acs.inorgchem.9b03409
Inorg. Chem. 2020, 59, 3753−3763

potential of the nickel is thus minimized, indeed almost indistinguishable from that of free NiN_2S_2.[29] Interestingly, there is an enhancement in the current intensity at the $Ni^{II/I}$ reduction event which would support the hypothesis of NiN_2S_2 ligand dissociation and the buildup of free NiN_2S_2 at the diffusion layer of the electrode. However (contrary to this hypothesis), such an enhancement of intensity has been observed in several examples of heterobimetallics containing the NiN_2S_2 metaloligand, which are highly unlikely to be dissociated.[12] We conjecture that some type of kinetic control (efficient electron transfer from electrode to the Ni center) governs this process in the intact bimetallic complexes.

To test the ability of complex **1** to respond electrochemically to added protons, cyclic voltammograms were recorded in the presence of trifluoroacetic acid (TFA) in CH_3CN. In the presence of 10 equiv of acid, the ν(CO) IR spectrum shows little change in pattern, indicating that complex **1** maintains its structural integrity (Figure 5). However, minor shifts (~7 cm^{-1}) toward more positive values are consistent with the protonated dangling thiolate (Figure 5). Computational DFT studies find that the HOMO of complex **1** is centered around the unbound thiolate sulfur, further indicating its potential to undergo protonation (Figure 6). The cyclic voltammogram of complex **1** upon sequential addition of aliquots of acid showed an increase in the cathodic current at the first reduction event at −1.82 V, which is presumed to be the Fe^IFe^I/Fe^IFe^0 reduction (Figure 7). Furthermore, a new, steadily increasing current event at −1.48 V can also be observed when increasing the concentration of acid in the medium (Figure 7). The attribution of the reduction-induced cathodic current enhancement upon addition of TFA to electrocatalytic H_2 production was verified by gas chromatography and quantified by bulk electrolysis experiments performed at −1.61 V for 30 min, in a CH_3CN solution containing 2 mM of catalyst and 50 equiv of TFA (TOF, 17.5 s^{-1}; TON, 0.22; FE, 78.4%; SI Figures S10−S16, Tables S1−S3). The plot of current heights of electrocatalytic waves vs acid concentration indicates steeper slopes for the event at −1.48 V compared to the all-CO starting material as well as (μ-pdt)[$Fe^I(CO)_3$][$Fe^I(CO)_2PPh_3$] (Figure 8), where the increase of sensitivity is on the order of **1** > (μ-pdt)[$Fe^I(CO)_3$][$Fe^I(CO)_2PPh_3$] > (μ-pdt)[[$Fe(CO)_3$]$_2$. Many reported mimics of [FeFe]-H_2ase show catalytic properties following reduction of the Fe center which makes it amenable to oxidatively add a proton converting it to a hydride.[21] Previous studies have shown that the all-CO complex is likely to have an EECC type electrocatalytic mechanism for proton reduction, especially at higher scan rates; at lower rates, there is a decomposition.[25,30] The monosubstituted (μ-pdt)[$Fe^I(CO)_3$][$Fe^I(CO)_3PPh_3$] displays a similar electrochemistry to that of complex **1** and shows a higher sensitivity toward the added acid compared to the all-CO complex.[25] The greater sensitivity of complex **1** to added acid compared to both the monophosphine substituted and the all-CO complexes is in agreement with the postulate that the metallodithiolato ligand might act as a pendant base. As a good donor, the NiN_2S_2 metallodithiolato ligand has the capability of increasing the electron density in the di-iron core and in addition will stabilize the oxidized center following the oxidative addition of a proton to the iron. In the monodentate

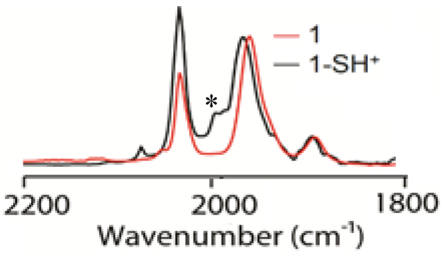

Figure 5. Overlay of IR spectra of **1** and $1H^+$ in CH_2Cl_2 solution. *Likely decomposition product.

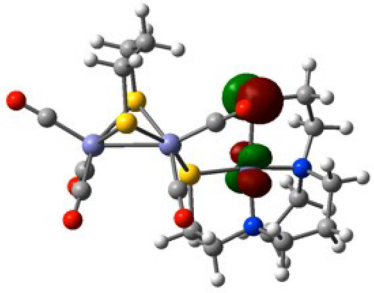

Figure 6. HOMO of complex **1**. See SI Table S1 for details.

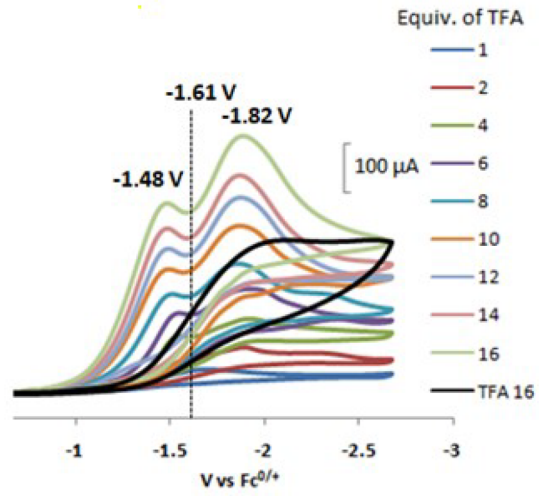

Figure 7. Cyclic voltammograms of **1** in 2 mM CH_3CN solution with added equivalents of TFA. The black trace shows 16 equiv of free TFA in the absence of a catalyst.

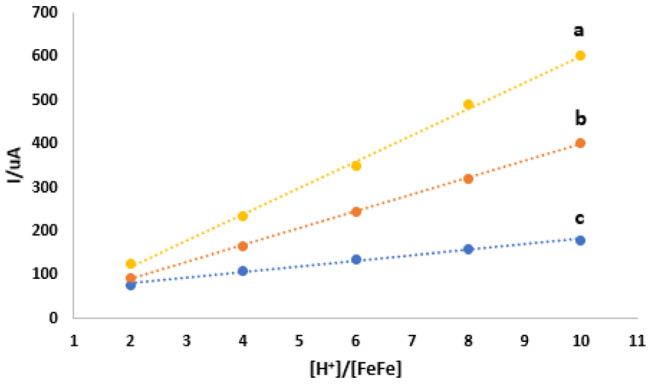

Figure 8. Dependence of current heights of electrocatalytic waves on acid concentration. (a) **1** (−1.48 V), (b) (μ-pdt)[$Fe(CO)_3$][$Fe(CO)_2PPh_3$] (−1.73 V), (c) (μ-pdt)[$Fe(CO)_3$]$_2$ (−1.95 V).

https://dx.doi.org/10.1021/acs.inorgchem.9b03409
Inorg. Chem. 2020, 59, 3753−3763

form, it harbors a nearby site for a proton to promote efficient proton/hydride coupling. It is interesting to note that complex **1** shows an increase of catalytic current at −1.48 V at lower pH values prior to the reduction in di-iron core. We postulate that at lower pH values protonation at unbound thiolate leads to the protonated complex **1H** which is capable of accepting an electron at a more positive reduction potential; this is arguably the first step toward the catalytic proton reduction, i.e., the "C" in C[ECEC]. Previous studies have shown that an electron-rich di-iron core may be protonated to yield an $Fe^{II}(\mu\text{-H})Fe^{II}$ bridging hydride.[21] Similarly, in complex **1**, the substituted iron has an increased electron density which we expect will take up a proton to yield a hydride-bound di-iron core at lower pH values probably via a concerted electron/proton transfer pathway; however, a pH dependent study is required to confirm this postulate. Computational studies have shown that complex **1H** has the capability to generate an asymmetric hydride localized on the iron with the bound NiN_2S_2 (**1HH**) where the $H^+\cdots H^-$ distance of 2.03 Å is favorable for coupling (Figure 9).

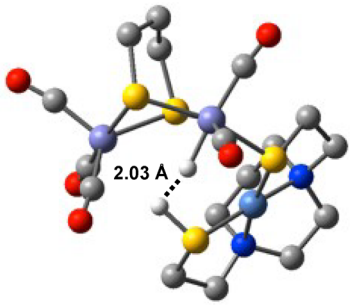

Figure 9. Modeled structure for complex **1HH**. See SI Table S2 for details.

Reactivity Studies Directed toward Evaluating FeFe−S_2N_2Ni Bond Strengths. In order to rank the Fe−S bond lability in the three FeFe complexes in different oxidation states of iron and bearing NiN_2S_2 metalloligands, complexes **1**, **2**, and **3** in CH_2Cl_2 solvent and at 25 °C were exposed to a 20-fold excess of PMe_3 (eqs 1, 2, and 3). Under these conditions, displacement of the NiN_2S_2 metalloligand in complex **1** yielding $(\mu\text{-pdt})[Fe(CO)_3][Fe(CO)_2PMe_3]$ (**1**-PMe_3) was complete within 15 min. Complex **2** more slowly converts to the PMe_3 analogue, requiring ≤2 h, and complex **3** shows no reaction whatsoever over the course of 3 h.

$$\text{complex } \mathbf{1} + PMe_3 \rightarrow (\mu\text{-pdt})[(Fe^{I}(CO)_3][Fe^{I}(CO)_2PMe_3] \quad (1)$$

$$\text{complex } \mathbf{2} + PMe_3 \rightarrow (\mu\text{-pdt})[Fe^{I}(CO)_3][\{Fe(NO)\}^{II}(IMe)(PMe_3)]^+BF_4^- \quad (2)$$

$$\text{complex } \mathbf{3} + PMe_3 \not\rightarrow (\mu\text{-pdt})(\mu\text{-H})[Fe^{II}(CO)_2(PME_3)][Fe^{II}(CO)(PMe_3)_2]^+PF_6^- \quad (3)$$

The disappearance of respective absorbances of complexes **1**, **2**, and **3** in the UV−vis spectra were used to monitor the reactions (Figure 10); mass spectrometry was used to identify both initial and final products (SI Figures S17−S19).

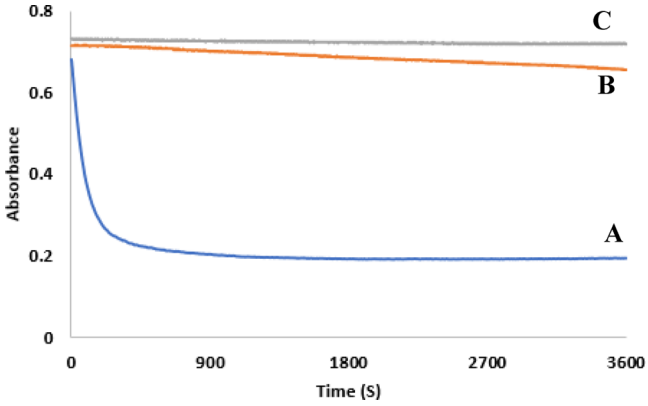

Figure 10. (A) Disappearance of absorbance at 393 nm for complex **1**, (B) 522 nm for complex **2**, (C) 442 nm for complex **3** in DCM.

A simplistic relationship of the qualitative results of NiN_2S_2 ligand displacement is with the expected electrostatic contribution to the Fe−S bonds in the metallodithiolato ligand: $Fe^IFe^I-S_2N_2Ni$ < $Fe^IFe^{II}-S_2N_2Ni$ < < $Fe^{II}Fe^{II}-S_2N_2Ni$. This correlation is assuming positive character of the NO-substituted Fe in complex **2** following the addition of NO^+, thus generating the Enemark−Feltham[31] $\{Fe(NO)\}^7$ unit as the NO^+ withdraws sufficient electron density from Fe^I, effectively generating $Fe^{II}(NO)^{\bullet}$. However, the steric encumbrance from the NHC ligand in complex **2** is also a factor as expressed in the longest Fe−S bond distance found, while the all-CO derivative, complex **1**, generates the shortest distance. The conundrum of steric vs electronic control thus encouraged further study.

The PMe_3/NiN_2S_2 exchange in complex **1** proceeds at a rate that is readily monitored by conventional techniques. We designed such studies in order to establish the mechanistic path and, if possible, to determine a kinetic measure of the FeFe−S_2N_2Ni bond strength.

Rates of NiN_2S_2/PMe_3 Ligand Exchange in Complex 1. Kinetic parameters for the reactions of **1** with PMe_3 were monitored by IR and UV−vis spectroscopies. For IR measurements, disappearance of the ν(CO) band at 1962 cm^{-1} with time was monitored and for UV−vis measurements; disappearance of the absorbance at 393 nm which corresponds to **1** was used, Figure 11.

In situ IR spectroscopy was initially used to identify the reactants and products. Due to the smaller requirement of sample concentration and faster spectral acquisition rates, UV−vis spectroscopy was used for the determination of rates as a function of temperature. The plots of $\ln(A_0/A_t)$ versus time showed good linearity as seen in Figure 12B. The derived values of k_{obs} at various PMe_3 concentrations and reaction temperatures, as determined by UV−vis spectroscopy, are given in SI Table S4, entries 1−12. Each k_{obs} was obtained from a single kinetic run, with at least ∼100 spectral accumulations per run. The plot of k_{obs} versus $[PMe_3]$, Figure 12A, shows linearity. However, a nonzero intercept indicates the reaction does not follow a strict second-order rate expression, but rather both associative (A) and dissociative (D) substitution processes are assumed to be involved, eq 4.

Hence, the plot of k_{obs} versus $[PMe_3]$ at 20 °C, Figure 12A and eq 5, yields the dissociative substitution rate constant, k_1 = 2.29 × 10^{-5} s^{-1}, derived from the intercept, and the rate constant for the associative path is obtained from the slope, k_2 = 4.90 × 10^{-3} M^{-1} s^{-1}.

https://dx.doi.org/10.1021/acs.inorgchem.9b03409
Inorg. Chem. 2020, 59, 3753−3763

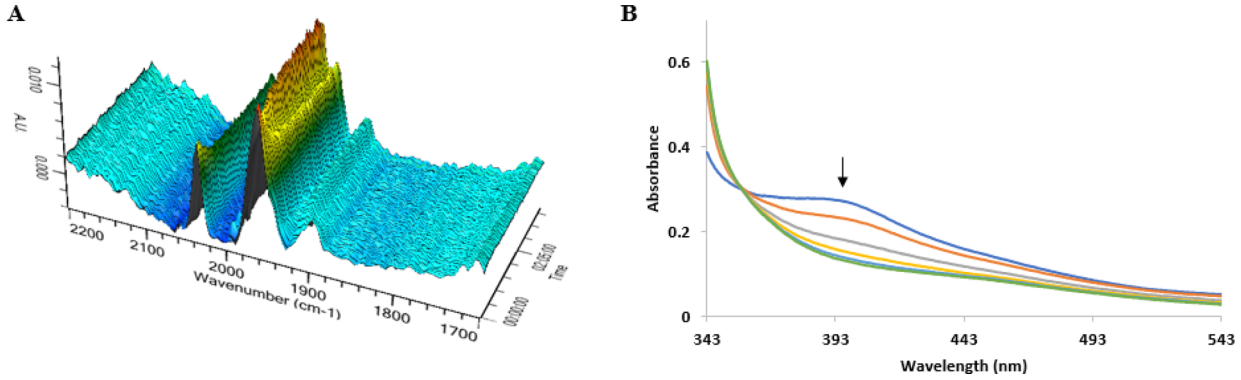

Figure 11. (a) Infrared spectra of 5 mM solution of **1** in DCM with 20-fold excess of PMe_3, in the 1800−2100 cm^{-1} region, as NiN_2S_2/PMe_3 exchange takes place to produce the complex **1**-PMe_3. (b) UV−vis spectra of converting 0.3 mM solution of complex **1** (initial: blue trace) to **1**-PMe_3 (final: green trace) in DCM.

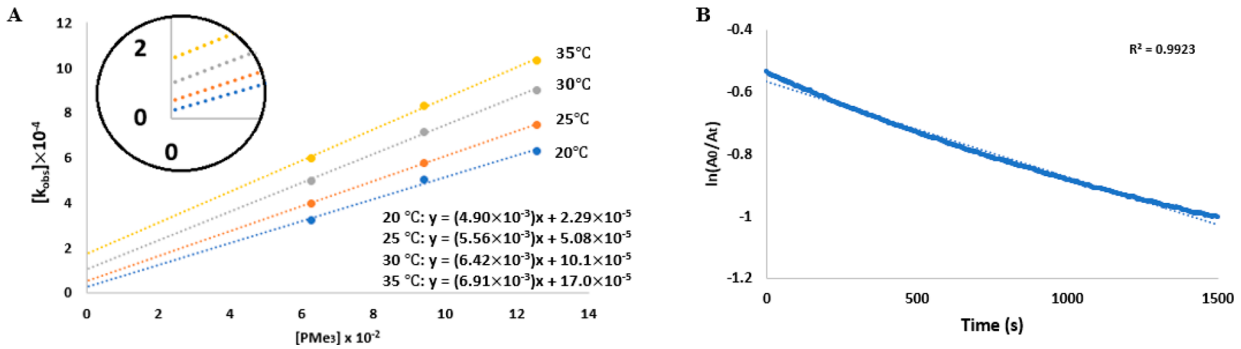

Figure 12. (a) Plots of k_{obs} vs [PMe_3] for the formation of **1**-PMe_3 from **1** measured at 20/25/30/35 °C (conditions: SI Table S4, entries 1−12). (b) Example plot of $\ln(A_0/A_t)$ vs time over four half-lives (conditions: SI Table S4, entry 1).

$$\text{rate} = k_1[\mathbf{1}] + k_2[\mathbf{1}][PMe_3] \quad (4)$$

$$\text{rate} = k_{obs}[\mathbf{1}];\ k_{obs} = k_1 + k_2[PMe_3] \quad (5)$$

The same reaction was monitored using in situ IR spectroscopy at −40 °C. The plot of k_{obs} vs [PMe_3] obtained from this data also resulted in a linear plot with nonzero intercept (SI Table S3, entries 1−3, Figure S14), confirming that the rate expression contains both associative and dissociative components. It should be noted that the IR and UV−vis traces represent a stoichiometric reaction, and reproducibility is on the order of 95%.

The temperature dependence of rate constants for both A and D pathways for the formation of complex **1**-PMe_3 from **1** obtained by UV−vis are given in Table 3 and presented graphically as Eyring plots, Figure 13. Extrapolation of Eyring plots led to a calculated value of $k_2 = 7.88 \times 10^{-3}$ M^{-1} s^{-1} and $k_1 = 1.31 \times 10^{-7}$ s^{-1} at −40 °C. These calculated values match the experimentally determined values for k_2 and k_1 at −40 °C using the in situ IR spectroscopic monitor (SI Table S3) within an acceptable margin, further confirming the accuracy of the method.

Calculated values for the enthalpy and entropy of activation are listed in Table 3. The small values of $\Delta H^{\ddagger}$ (15 (±1) kJ/mol) and large negative values for $\Delta S^{\ddagger}$ (−237 (±5) J/mol·K) are consistent with the associative pathway. Equation 6 describes the PMe_3/CO substitution reaction of a monosubstituted phosphine complex, affording a disubstituted phosphine complex.

Table 3. Temperature Dependence of Reaction of PMe_3 with 1

rxn path	T, °C	k	activation parameters[b]
1 → **1**-PMe_3[a] (A path)		$10^{-3}k_2$, M^{-1} s^{-1}	
	20	4.90	E_a = 17 kJ/mol
	25	5.56	$\Delta H^{\ddagger}$ = 15 (±1) kJ/mol
	30	6.42	$\Delta S^{\ddagger}$ = −237 (±5) J/mol.K
	35	6.91	$\Delta G^{\ddagger}$ = 86 kJ/mol (298 K)
		$10^{-4}k_1$, s^{-1}	
1 → **1**-PMe_3[a] (D path)	20	0.23	E_a = 101 kJ/mol
	25	0.51	$\Delta H^{\ddagger}$ = 98 (±5) kJ/mol
	30	1.01	$\Delta S^{\ddagger}$ = 3 (±17) J/mol.K
	35	1.70	$\Delta G^{\ddagger}$ = 97 kJ/mol (298 K)

[a][a] = 3.1 × 10^{-4} M; [PMe_3] = 0.0627−0.1254 M. [b]Errors in activation parameters reported at 95% confidence level.

$$(\mu\text{-pdt})[Fe^{I}(CO)_3][Fe^{I}(CO)_2PMe_3] + PMe_3 \xrightarrow{E_{act}} (\mu\text{-pdt})[Fe(CO)_2(PMe_3)]_2 \quad (6)$$

This reaction was previously reported to follow a similar associative pathway;[20] however, the reported activation energy barrier for the CO displacement reaction is higher compared to the PMe_3 substitution reaction of NiN_2S_2 in **1**.[20] This is possibly due to the fact that the NiN_2S_2 ligand, according to the ν(CO) IR data, is a better electron donor compared to PMe_3 (Table 1). The proposed mechanism for such reactions (Scheme 2) specifies that E_{act}(overall) is composed of two contributory factors: E_{act}(attack) and E_{act}(rot'n).[18] Accepting

https://dx.doi.org/10.1021/acs.inorgchem.9b03409
Inorg. Chem. 2020, 59, 3753−3763

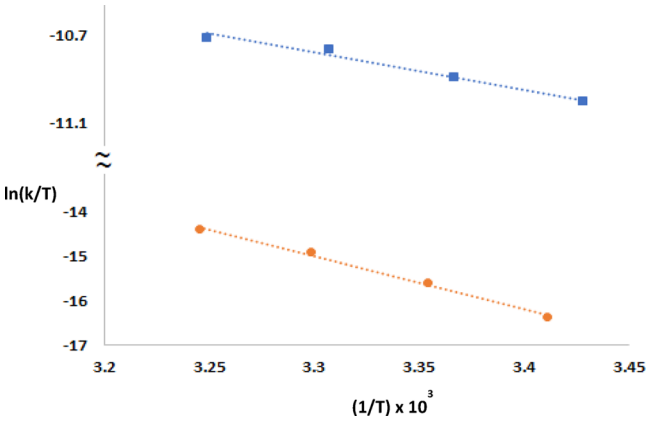

Figure 13. Eyring plots for the formation of complex **1**-PMe_3 from the associative (■) and dissociative (●) paths.

this analysis, we conclude that during the associative pathway, PMe_3 attacks the more electrophilic $[Fe(CO)_3]$ center, leading to shift one of its CO's underneath the Fe−Fe vector (rotation of the $Fe(CO)_3$ unit) where it is stabilized by the electron-rich side to create the transition state (Scheme 2). Due to the assistance from the $[Fe(CO)_2{\cdot}NiN_2S_2]$ center to stabilize the rotated transition state, the contribution from E_{act}(rot'n) becomes significantly smaller, thereby lowering the E_{act}(overall) compared to the reaction described by eq 6.[20]

Large values of $\Delta H^{\ddagger}$ and positive values for $\Delta S^{\ddagger}$ are hallmarks for dissociative pathways. The dissociative path for the reaction between **1** and PMe_3 yields a $\Delta H^{\ddagger}$ value of 98 kJ/mol, possibly due to the detachment of the NiN_2S_2 ligand from the di-iron core, which is preparatory to the transition state, which permits the attachment of the incoming PMe_3 ligand (Scheme 3). Thus, we conclude that for complex **1** the Fe−S bond energy is ca. 98 kJ/mol.

■ CONCLUSIONS

The metallodithiolato ligand (NiN_2S_2) efficiently replaces phosphines or even π-acid ligands such as CN^- or CO in binding to the propanedithiolate bridged di-iron scaffold, a famous precursor to numerous biomimetics of the [FeFe]-H_2ase active site. The $[FeFe]{\cdot}NiN_2S_2$ trimetallics were characterized in three redox states, $[Fe^IFe^I]$ (**1**), $[Fe^I[Fe(NO)]^{II}]$ (**2**), and $[(\mu\text{-H})Fe^{II}Fe^{II}]$ (**3**), using IR spectroscopy, ESI-MS, and X-ray crystallography. In all, the *cis*-dithiolate, NiN_2S_2, displays monodentate binding using one sulfur, while the unbound thiolate has the potential to act as a pendant base, modeling the bridge-head amine of the [FeFe] enzyme active site or the terminal cysteinyl thiolate in the [NiFe]-H_2ase active site. Interestingly, in no case were we successful in generating the bidentate form of complex **1**·NiN_2S_2. Electrochemical studies of complex **1** in the presence of added equivalents of trifluoraacetic acid showed a catalytic current response with the formation of a new event at −1.48 V, which is prior to the reduction of the di-iron core. This, we posit, is due to the protonation at free thiolate, which makes the trimetallic complex more susceptible to reduction. Furthermore, complex **1** shows higher sensitivity toward the added acid compared to $(\mu\text{-pdt})[[Fe(CO)_3]_2$ and $(\mu\text{-pdt})[Fe^I(CO)_3][Fe^I(CO)_3PPh_3]$. This result is taken as consistent with unbound thiolate acting as a pendant base that assists in guiding the proton toward the di-iron core. Ligand substitution studies indicate the ability of metallodithiolato ligand to undergo substitution reactions in the presence of the PMe_3 ligand according to a dual, associative + dissociative pathway; the dissociative path provided activation parameters giving a kinetic measure of the Fe−S bond strength of ca. 98 kJ/mol. Thus, for synthetic purposes, such metallodithiolato ligands can add to the organometallic ligand tool box with features[32] that give flexibility in positioning a second nucleophilic site.

■ EXPERIMENTAL SECTION

Methods and Materials. An MBraun Manual Solvent Purification System with Alcoa F200 activated alumina desiccant was used to purify dichloromethane (CH_2Cl_2), acetonitrile (CH_3CN), tetrahydrofuran (THF), hexane, and diethyl ether. All reactions and operations were carried out using standard Schlenk conditions under a N_2 atmosphere. All regents were used as received from standard vendors unless otherwise stated. The known complexes $(\mu\text{-pdt})[Fe(CO)_3]_2$, $(\mu\text{-pdt})[Fe(CO)_3][(Fe(NO))^{II}(IMe)(CO)]^+BF_4^-$, $(\mu\text{-pdt})(\mu\text{-H})[Fe^{II}(CO)_2(PMe_3)]_2^+PF_6^-$, and Ni(bme-dach) (bme-dach = [N,N′-bis(2-mercaptidoethyl)-1,4-diazacycloheptane] nickel-(II) were prepared according to the literature procedures.[22,33]

Physical Measurements. The Bruker Tensor 37 Fourier transform IR (FTIR) spectrometer was used to record solution infrared spectra, using a CaF_2 cell with a 0.2 mm path length. Kinetic measurements using solution infrared spectroscopy were carried out and recorded on a Bruker Tensor 27 FTIR spectrometer. UV−vis measurements were obtained using a Shimadzu UV-2450 UV−vis spectrophotometer. Eyela PSL-1400 and VWR polyscience 1162 instruments were used as a controlled temperature baths in kinetic experiments. The Texas A&M Laboratory for Biological Mass Spectrometry performed all mass spectrometry. The Atlantic Microlab Inc. located in Norcross, Georgia, performed all elemental analyses. $^1H/^{31}P$ NMR were recorded on the Bruker 400 MHz superconducting NMR instrument.

X-ray Diffraction Analysis. The crystal data for **1**, **2**, and **3** were determined using a Bruker Apex 2 X-ray (three-circle) diffractometer with a Mo sealed X-ray tube ($K\alpha$ = 0.70173 Å) at 110 K. Weighted least-squares refinement on F^0 was used for refining the structures. At idealized positions, hydrogen atoms were placed, and fixed isotropic

Scheme 2. Proposed Mechanism for the Associative Path

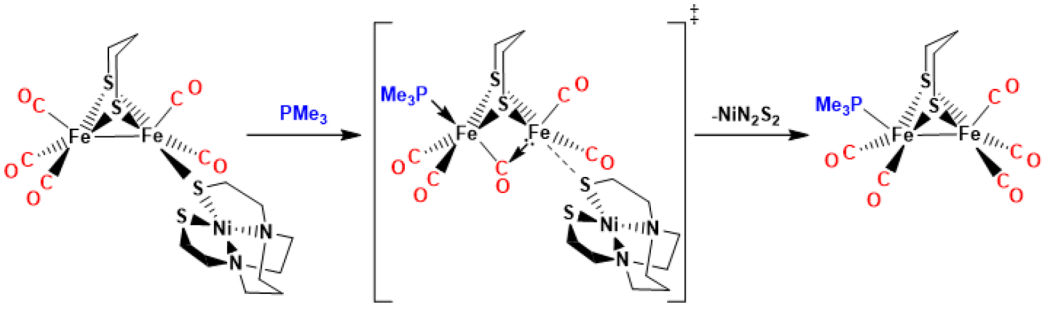

https://dx.doi.org/10.1021/acs.inorgchem.9b03409
Inorg. Chem. 2020, 59, 3753−3763

Scheme 3. Dissociative Path for PMe_3/NiN_2S_2 Exchange

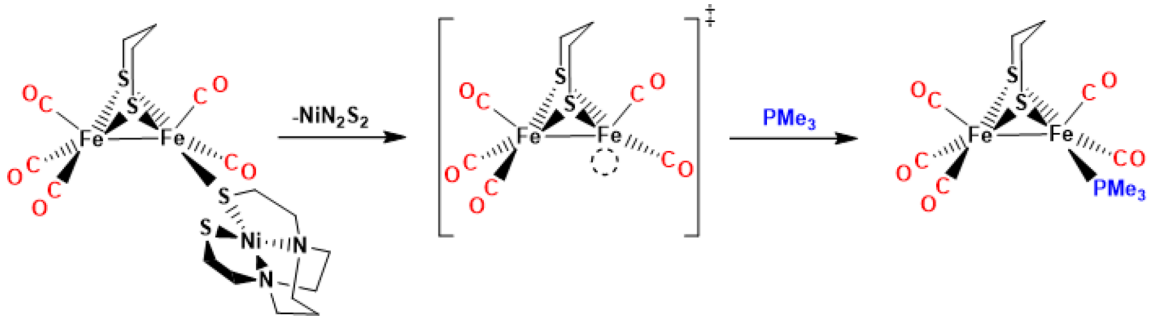

displacement parameters were used to refine them. Anisotropic displacement parameters were employed for all non-hydrogen atoms. The following programs were used: data collection, APEX3; data reduction, SAINT; absorption correction, SADABS; and cell refinement and structure solutions, SHELXS/XT. The final data presentation and structure plots were generated in Olex2.30. Crystallographic data for the complexes **1**, **2**, and **3** are deposited in the Cambridge Crystallographic Data Centre; their numbers are CCDC 1965616 (**1**), CCDC 1965614 (**2**), and CCDC 1965615 (**3**). Crystal data and structure refinement parameters are summarized in SI Tables S5, S6, and S7.

Electrochemistry. A custom-made three-necked conical shaped flask with an outlet port/gas inlet equipped with a three-electrode setup was used to obtain cyclic voltammograms (CVs) using a CH1600E electrochemical analyzer (HCH instruments, Inc.). The working electrode was a 0.071 cm^2 glassy carbon dish electrode. The counter electrode was a platinum wire, and the reference electrode was Ag/Ag^+ using a $AgNO_3$ 1 mM solution in CH_3CN in a Vycor-tipped glass tube. Diamond paste (3 μm) was used to polish the working electrode, and a blanket of Ar was maintained over the solution throughout the experiment following an initial Ar purge for 5 min. All CVs were obtained in CH_3CN at room temperature using 0.1 M $[n\text{-}Bu_4N][PF_6]$ as the electrolyte and 2.0 mM in analyte. All potentials were shown relative to the Fc/Fc+ couple at 0.00 V. Bulk electrolysis experiments were conducted using a 3 mm glassy carbon working electrode, a Ni−Cr coiled wire counter electrode, and a 1 mM $Ag/AgNO_3(CH_3CN)$ reference electrode. The electrochemical cell was charged with 10 mL of 0.1 M $[n\text{-}Bu_4N][PF_6]$ in CH_3CN and purged with Ar to deplete O_2. To the cell, 2×10^{-5} mol of the catalyst and 50 equiv of trifluoracetic acid (TFA) were added. CV was recorded in order to ensure the experiment was under catalytic conditions, and the bulk electrolysis was performed at −1.61 V vs Fc/Fc^+ for 1 h. The overhead gas was analyzed using gas chromatography (GC) to detect H_2 (SI Figures S10, S11).

Kinetic Measurements. Pseudo-first-order reaction conditions were employed for determination of the order of the reaction. Reactions were monitored using infrared spectroscopy and UV−vis. For IR measurements, 2 mL of DCM solution containing 4.7 mmolar di-iron complex **1** in a two-neck flask was placed in a temperature-controlled bath. Following temperature equilibration, a solution of PMe_3 at the same temperature was injected into the two-neck flask. While being magnetically stirred, aliquots for IR spectra were removed, and the reaction was monitored through four half-lives. Rates of reactions were measured by following the decrease in absorption of the reactant's most intense nonoverlapping ν(CO) vibration, which was centered at ca. 1966 cm^{-1}. The IR data were reproduced using UV−vis spectroscopy where the reactions were monitored in a cuvette. Three milliliters of 0.3 mmolar di-iron complex in DCM was directly injected with the PMe_3 solution, and a decrease of the peak at 393 nm, which corresponds to the starting material, was monitored. Rate constants were calculated from plots of $\ln(A_0/A_t)$ versus time typically using >30 data points over four to five half-lives, giving a correlation constant of 0.99. Reproducibility of a run under identical conditions was 95% or better. Activation parameters $\Delta H^{\ddagger}$ and $\Delta S^{\ddagger}$ were obtained from Eyring plots; activation energies, E_a, were obtained from Arrhenius plots (SI Figures S12−S19, Tables S3 and S4).

Synthesis. Three new complexes containing a di-iron unit and NiN_2S_2 were prepared, isolated, and characterized.

*(μ-pdt)[($Fe^{I}(CO)_3$][$Fe^{I}(CO)_2$·NiN_2S_2] (**1**).* A solution of (μ-pdt)[Fe$(CO)_3]_2$ (386 mg, 1.00 mmol), NiN_2S_2 (277 mg, 1.00 mmol), and trimethylamine N-oxide (TMANO; 75 mg, 1.00 mmol) in CH_2Cl_2 (20 mL) was stirred for 30 min at ca. 22 °C. The resulting solution was dried under a vacuum and washed with 20 mL (×3) of hexane. The mixture was redissolved in CH_2Cl_2 and filtered through Celite to remove any unreacted starting material, and X-ray quality crystals for complex **1** were obtained by layering moderately concentrated solutions in CH_2Cl_2 with hexanes at −28 °C under a N_2 atmosphere.

IR (CH_2Cl_2, cm^{-1}): ν(CO) 2032, 1962, 1900. ESI-MS^+: m/z 633.85 (calcd for $[M]^+$, 633.86). Elem anal. calcd (found) for $C_{17}H_{24}Fe_2N_2NiO_5S_4$ (MW = 635.01 g mol^{-1}): C, 32.15 (32.21); H, 3.81 (3.90); N, 4.41 (4.52). ^1H NMR (400 MHz, CD_2Cl_2): δ 2.00−4.50 (18H), 1.56 (4H), 1.27 (2H) (SI Figures S1, S4, S7).

*(μ-pdt)[$Fe^{I}(CO)_3$][($Fe(NO))^{II}$(IMe)(CO)]$^+$ BF_4^- (**2**).* A solution of (μ-pdt)[Fe$(CO)_3$][($Fe(NO))^{II}$(IMe)(CO)]$^+$ BF_4^- (543 mg, 1.00 mmol) and NiN_2S_2 (277 mg, 1.00 mmol) in CH_2Cl_2 (20 mL) was stirred for 3 h at room temperature. The resulting solution was dried under a vacuum and washed with 20 mL (×3) of diethyl ether. The mixture was redissolved in CH_2Cl_2 and filtered through Celite to remove any unreacted starting material, and X-ray quality crystals for complex **2** were obtained by layering moderately concentrated solutions in CH_2Cl_2 with hexane and ether (3:1) at −28 °C under N_2. IR (CH_2Cl_2, cm^{-1}): ν(CO) 2056, 1990; ν(NO) 1740. ESI-MS^+: m/z 703.93 (calcd for $[M]^+$, 703.94). Elem anal. calcd (found) for $C_{20}H_{32}Fe_2N_5NiO_4S_4BF_4$ (MW = 791.93 g mol^{-1}): C, 30.33 (30.95); H, 4.07 (3.92); N, 8.84 (8.17) (SI Figures S2, S5)

*(μ-pdt)(μ-H)[$Fe^{II}(CO)_2(PMe_3)$][$Fe^{II}(CO)(PMe_3)$·NiN_2S_2]$^+BF_4^-$ (**3**).* A solution of (μ-pdt)(μ-H)[$Fe^{II}(CO)_2(PMe_3)]_2^+$ PF_6^- (570 mg, 1.00 mmol) and NiN_2S_2 (277 mg, 1.00 mmol) in CH_2Cl_2 (20 mL) was stirred for 30 min at room temperature while irradiated by a sunlamp. The resulting solution was dried under a vacuum and washed with 20 mL (×3) of hexane. The mixture was redissolved in CH_2Cl_2 and filtered through Celite to remove any decomposed products. An equimolar CH_2Cl_2 solution of sodium tetrakis[3,5-bis-(trifluoromethyl)phenyl]borate (Sodium BAr^{F-}) (886 mg, 1.00 mmol) was added to the above solution and stirred for 1 h. The final solution was filtered over Celite to remove Na PF_6^-. X-ray quality crystals for complex **3** as its BAr^{F-} salt were obtained by layering moderately concentrated solutions in CH_2Cl_2 with hexanes at −28 °C under N_2.

IR (CH_2Cl_2, cm^{-1}): ν(CO) 2023, 1968, 1929. ESI-MS^+: m/z 730.95 (calcd for $[M]^+$, 730.97). Elem anal. calcd (found) for $C_{21}H_{43}Fe_2N_2NiO_3P_2S_4BF_4$ (MW = 818.96 g mol^{-1}): C, 30.80 (31.00); H, 5.29 (5.40); N, 3.42 (3.76). ^{31}P NMR (400 MHz, dimethyl sulfoxide-d_6): δ 21.13 (PMe_3, [Fe$(CO)_2PMe_3$]), −8.69 (PMe_3, [Fe(CO)(PMe_3)(NiN_2S_2)]; PF_6^-, −144.24; SI Figures S3, S6, S8).

https://dx.doi.org/10.1021/acs.inorgchem.9b03409
Inorg. Chem. 2020, 59, 3753−3763

■ ASSOCIATED CONTENT

Supporting Information

The Supporting Information is available free of charge at https://pubs.acs.org/doi/10.1021/acs.inorgchem.9b03409.

FTIR spectra of **1**, **2**, and **3**; ESI+ mass spectra of **1**, **2**, and **3**; ^{1}H NMR spectrum of **1**; ^{31}P NMR spectrum of **3**; cyclic voltammetry of **1**; bulk electrolysis of **1**; gas chromatogram of the bulk electrolysis product of **1**; absorbance vs time plot for complex **1**; IR characterization of products after UV−vis kinetics for complex **1**; rate data for the reaction of PMe_3 with **1** at −40 °C in DCM using IR; plot of k_{obs} vs [PMe_3] for the formation of **1**-PMe_3 at −40 °C; rate data for the reaction of PMe_3 with **1** at 20/25/30/35 °C in DCM using UV−vis; ESI+ mass spectrum for the reaction between **2** and PMe_3 after 1 h; ESI+ mass spectrum for the reaction between **2** and PMe_3 after 2 h; ESI+ mass spectrum for the reaction between **3** and PMe_3 after 3 h; thermal ellipsoid at 50% probability for **1**, **2**, and **3**; crystal data and structure refinement for **1**, **2**, and **3** (PDF)

Accession Codes

CCDC 1965614−1965616 contain the supplementary crystallographic data for this paper. These data can be obtained free of charge via www.ccdc.cam.ac.uk/data_request/cif, or by emailing data_request@ccdc.cam.ac.uk, or by contacting The Cambridge Crystallographic Data Centre, 12 Union Road, Cambridge CB2 1EZ, UK; fax: +44 1223 336033.

■ AUTHOR INFORMATION

Corresponding Authors

Donald J. Darensbourg − *Department of Chemistry, Texas A&M University, College Station, Texas 77843, United States;* orcid.org/0000-0001-9285-4895; Email: djdarens@chem.tamu.edu

Marcetta Y. Darensbourg − *Department of Chemistry, Texas A&M University, College Station, Texas 77843, United States;* orcid.org/0000-0002-0070-2075; Email: marcetta@chem.tamu.edu

Authors

Kavindu Dilshan Kariyawasam Pathirana − *Department of Chemistry, Texas A&M University, College Station, Texas 77843, United States*

Pokhraj Ghosh − *Department of Chemistry, Texas A&M University, College Station, Texas 77843, United States*

Chung-H. Hsieh − *Department of Chemistry, Tamkang University, New Taipei City, Taiwan*

Lindy Chase Elrod − *Department of Chemistry, Texas A&M University, College Station, Texas 77843, United States;* orcid.org/0000-0002-5583-2731

Nattamai Bhuvanesh − *Department of Chemistry, Texas A&M University, College Station, Texas 77843, United States*

Complete contact information is available at: https://pubs.acs.org/10.1021/acs.inorgchem.9b03409

Notes

The authors declare no competing financial interest.

■ ACKNOWLEDGMENTS

This work was financially supported by the National Science Foundation (CHE-1665258) and the Robert A. Welch Foundation (A-0924 to M.Y.D. and A-0923 to D.J.D.)

■ ABBREVIATIONS

A path, Associative path; D path, Dissociative path; TOF, turnover frequency; TON, turnover number; FE, Faradaic efficiency

■ REFERENCES

(1) Lubitz, W.; Ogata, H.; Rüdiger, O.; Reijerse, E. Hydrogenases. *Chem. Rev.* **2014**, *114* (8), 4081−4148.

(2) Schilter, D.; Camara, J. M.; Huynh, M. T.; Hammes-Schiffer, S.; Rauchfuss, T. B. Hydrogenase Enzymes and Their Synthetic Models: The Role of Metal Hydrides. *Chem. Rev.* **2016**, *116* (15), 8693−8749.

(3) Darensbourg, M. Y. Hydrogenase Active Sites: a New Paradigm for Natural Product-Inspired Synthesis Based on Organometallic Chemistry. *Comments Inorg. Chem.* **2010**, *31* (3−4), 144−152.

(4) Liu, T.; Darensbourg, M. Y. A Mixed-Valent, Fe(II)Fe(I), Diiron Complex Reproduces the Unique Rotated State of the [FeFe]-Hydrogenase Active Site. *J. Am. Chem. Soc.* **2007**, *129* (22), 7008−7009.

(5) Li, Y.; Rauchfuss, T. B. Synthesis of Diiron(I) Dithiolato Carbonyl Complexes. *Chem. Rev.* **2016**, *116* (12), 7043−7077.

(6) Peters, J. W.; Lanzilotta, W. N.; Lemon, B. J.; Seefeldt, L. C. X-ray Crystal Structure of the Fe-Only Hydrogenase (CpI) from *Clostridium pasteurianum* to 1.8 Angstrom Resolution. *Science* **1998**, *282* (5395), 1853−1858.

(7) Volbeda, A.; Charon, M.-H.; Piras, C.; Hatchikian, E. C.; Frey, M.; Fontecilla-Camps, J. C. Crystal structure of the nickel−iron hydrogenase from Desulfovibrio gigas. *Nature* **1995**, *373* (6515), 580−587.

(8) Henry, R. M.; Shoemaker, R. K.; DuBois, D. L.; DuBois, M. R. Pendant Bases as Proton Relays in Iron Hydride and Dihydrogen Complexes. *J. Am. Chem. Soc.* **2006**, *128* (9), 3002−3010.

(9) Chiang, C.-Y.; Miller, M. L.; Reibenspies, J. H.; Darensbourg, M. Y. Bismercaptoethanediazacyclooctane as a N2S2 Chelating Agent and Cys−X−Cys Mimic for Fe(NO) and Fe(NO)2. *J. Am. Chem. Soc.* **2004**, *126* (35), 10867−10874.

(10) Denny, J. A.; Darensbourg, M. Y. Metallodithiolates as Ligands in Coordination, Bioinorganic, and Organometallic Chemistry. *Chem. Rev.* **2015**, *115* (11), 5248−5273.

(11) Rao, P. V.; Bhaduri, S.; Jiang, J.; Holm, R. H. Sulfur Bridging Interactions of Cis-Planar NiII−S2N2 Coordination Units with Nickel(II), Copper(I,II), Zinc(II), and Mercury(II): A Library of Bridging Modes, Including NiII(μ2-SR)2MI,II Rhombs. *Inorg. Chem.* **2004**, *43* (19), 5833−5849.

(12) Ghosh, P.; Ding, S.; Chupik, R. B.; Quiroz, M.; Hsieh, C.-H.; Bhuvanesh, N.; Hall, M. B.; Darensbourg, M. Y. A matrix of heterobimetallic complexes for interrogation of hydrogen evolution reaction electrocatalysts. *Chemical Science* **2017**, *8* (12), 8291−8300.

(13) Brazzolotto, D.; Gennari, M.; Queyriaux, N.; Simmons, T. R.; Pécaut, J.; Demeshko, S.; Meyer, F.; Orio, M.; Artero, V.; Duboc, C. Nickel-centred proton reduction catalysis in a model of [NiFe] hydrogenase. *Nat. Chem.* **2016**, *8*, 1054.

(14) Nguyen, N. T.; Mori, Y.; Matsumoto, T.; Yatabe, T.; Kabe, R.; Nakai, H.; Yoon, K.-S.; Ogo, S. A [NiFe]hydrogenase model that catalyses the release of hydrogen from formic acid. *Chem. Commun.* **2014**, *50* (87), 13385−13387.

(15) Brazzolotto, D.; Wang, L.; Tang, H.; Gennari, M.; Queyriaux, N.; Philouze, C.; Demeshko, S.; Meyer, F.; Orio, M.; Artero, V.; Hall, M. B.; Duboc, C. Tuning Reactivity of Bioinspired [NiFe]-Hydrogenase Models by Ligand Design and Modeling the CO Inhibition Process. *ACS Catal.* **2018**, *8* (11), 10658−10667.

(16) Ghosh, P.; Quiroz, M.; Wang, N.; Bhuvanesh, N.; Darensbourg, M. Y. Complexes of MN2S2·Fe(η5-C5R5)(CO) as platform for exploring cooperative heterobimetallic effects in HER electrocatalysis. *Dalton Transactions* **2017**, *46* (17), 5617−5624.

(17) Ding, S.; Ghosh, P.; Darensbourg, M. Y.; Hall, M. B. Interplay of hemilability and redox activity in models of hydrogenase active sites. *Proc. Natl. Acad. Sci. U. S. A.* **2017**, *114* (46), E9775−E9782.

(18) Darensbourg, M. Y.; Lyon, E. J.; Zhao, X.; Georgakaki, I. P. The organometallic active site of [Fe]hydrogenase: Models and entatic states. *Proc. Natl. Acad. Sci. U. S. A.* **2003**, *100* (7), 3683.
(19) Lyon, E. J.; Georgakaki, I. P.; Reibenspies, J. H.; Darensbourg, M. Y. Coordination Sphere Flexibility of Active-Site Models for Fe-Only Hydrogenase: Studies in Intra- and Intermolecular Diatomic Ligand Exchange. *J. Am. Chem. Soc.* **2001**, *123* (14), 3268−3278.
(20) Li, B.; Liu, T.; Singleton, M. L.; Darensbourg, M. Y. Influence of Sulf-Oxygenation on CO/L Substitution and Fe(CO)3 Rotation in Thiolate-Bridged Diiron Complexes. *Inorg. Chem.* **2009**, *48* (17), 8393−8403.
(21) Zhao, X.; Georgakaki, I. P.; Miller, M. L.; Mejia-Rodriguez, R.; Chiang, C.-Y.; Darensbourg, M. Y. Catalysis of H2/D2 Scrambling and Other H/D Exchange Processes by [Fe]-Hydrogenase Model Complexes. *Inorg. Chem.* **2002**, *41* (15), 3917−3928.
(22) Bethel, R. D.; Crouthers, D. J.; Hsieh, C.-H.; Denny, J. A.; Hall, M. B.; Darensbourg, M. Y. Regioselectivity in Ligand Substitution Reactions on Diiron Complexes Governed by Nucleophilic and Electrophilic Ligand Properties. *Inorg. Chem.* **2015**, *54* (7), 3523−3535.
(23) Rampersad, M. V.; Jeffery, S. P.; Golden, M. L.; Lee, J.; Reibenspies, J. H.; Darensbourg, D. J.; Darensbourg, M. Y. Characterization of Steric and Electronic Properties of NiN2S2 Complexes as S-Donor Metallodithiolate Ligands. *J. Am. Chem. Soc.* **2005**, *127* (49), 17323−17334.
(24) Rampersad, M. V.; Jeffery, S. P.; Reibenspies, J. H.; Ortiz, C. G.; Darensbourg, D. J.; Darensbourg, M. Y. N2S2Ni Metallothiolates as a Class of Ligands that Support Organometallic and Bioorganometallic Reactivity. *Angew. Chem.* **2005**, *117* (8), 1243−1246.
(25) Chong, D.; Georgakaki, I. P.; Mejia-Rodriguez, R.; Sanabria-Chinchilla, J.; Soriaga, M. P.; Darensbourg, M. Y. Electrocatalysis of hydrogen production by active site analogues of the iron hydrogenase enzyme: structure/function relationships. *Dalton Transactions* **2003**, No. 21, 4158−4163.
(26) Liu, T.; Li, B.; Singleton, M. L.; Hall, M. B.; Darensbourg, M. Y. Sulfur Oxygenates of Biomimetics of the Diiron Subsite of the [FeFe]-Hydrogenase Active Site: Properties and Oxygen Damage Repair Possibilities. *J. Am. Chem. Soc.* **2009**, *131* (23), 8296−8307.
(27) Li, P.; Wang, M.; He, C.; Liu, X.; Jin, K.; Sun, L. Phosphane and Phosphite Unsymmetrically Disubstituted Diiron Complexes Related to the Fe-Only Hydrogenase Active Site. *Eur. J. Inorg. Chem.* **2007**, *2007* (23), 3718−3727.
(28) Farmer, P. J.; Reibenspies, J. H.; Lindahl, P. A.; Darensbourg, M. Y. Effects of sulfur site modification on the redox potentials of derivatives of [N,N′-bis(2-mercaptoethyl)-1,5-diazacyclooctanato]-nickel(II). *J. Am. Chem. Soc.* **1993**, *115* (11), 4665−4674.
(29) Zhao, T.; Ghosh, P.; Martinez, Z.; Liu, X.; Meng, X.; Darensbourg, M. Y. Discrete Air-Stable Nickel(II)−Palladium(II) Complexes as Catalysts for Suzuki−Miyaura Reactions. *Organometallics* **2017**, *36* (9), 1822−1827.
(30) Trautwein, R.; Almazahreh, L. R.; Görls, H.; Weigand, W. Steric effect of the dithiolato linker on the reduction mechanism of [Fe2(CO)6{μ-(XCH2)2CRR′}] hydrogenase models (X = S, Se). *Dalton Transactions* **2015**, *44* (43), 18780−18794.
(31) Enemark, J. H.; Feltham, R. D. Principles of structure, bonding, and reactivity for metal nitrosyl complexes. *Coord. Chem. Rev.* **1974**, *13* (4), 339−406.
(32) Denny, J. A.; Darensbourg, M. Y. Approaches to quantifying the electronic and steric properties of metallodithiolates as ligands in coordination chemistry. *Coord. Chem. Rev.* **2016**, *324*, 82−89.
(33) Smee, J. J.; Miller, M. L.; Grapperhaus, C. A.; Reibenspies, J. H.; Darensbourg, M. Y. Subtle Bite-Angle Influences on N2S2Ni Complexes. *Inorg. Chem.* **2001**, *40* (14), 3601−3605.

https://dx.doi.org/10.1021/acs.inorgchem.9b03409
Inorg. Chem. 2020, 59, 3753−3763